Asymmetric supercapacitor based on nanostructured graphene foam/ polyvinyl alcohol /formaldehyde and activated carbon electrodes

Bello Abdulhakeem*, Barzegar Farshad, Momodu Damilola, Dangbegnon Julien, Taghizadeh Fatemeh, Fabiane Mopeli, and Manyala Ncholu*

Department of Physics, Institute of Applied Materials, SARChI Chair in Carbon Technology and Materials,University of Pretoria, Pretoria 0028, South Africa.

*Corresponding author. E-mail address: ncholu.manyala@up.ac.za and bellohakeem@gmail.com

Tel.: +27 012 420 3549; Fax: +27 012 420 2516 (N. Manyala)

ABSTRACT

We present the electrochemical results of highly porous and interconnected carbon material by activation of graphene foam/polyvinyl alcohol-formaldehyde composite material designated as GF/PVA-F. Asymmetric supercapacitor devices were fabricated using the activated material (GF/PVA-F) and activated carbon (AC) as the positive and negative electrodes respectively. The device exhibited a maximum energy density of 42 mWh cm^{-2}, a power density of 0.5 W cm^{-2} and 98% retention of its initial capacitance after 2000 cycles in an extended cell potential window of 1.8 V in 1 M Na_2SO_4 aqueous electrolyte. This work shows the great potential of this material for high performance energy storage application.

KEYWORDS: Graphene foam, polyvinyl alcohol, formaldehyde, KOH activation, asymmetric supercapacitor

1 INTRODUCTION

The recent boom and increasing demand in portable electronic devices requires high power and energy storage devices. Electrochemical capacitors (ECs) also known as supercapacitors represent an emerging class of energy-storage devices and are suitable for such application due to their high power density and excellent cycle life [1,2]. They are differentiated from their storage counterparts by their ability to store charge at electrochemical interfaces which gives rise to effective capacitance orders of magnitude higher than those obtained by storing charge in an electric field applied across a conventional dielectric material [3]. ECs have the ability to release the stored energy over timescales of a few seconds and exhibit excellent cycle life (thousands of cycles) which represents an advantage over batteries [3]. The design of asymmetric supercapacitors (ASCs) has been shown to be an effective method for the integration of different capacitive or pseudocapacitive electrode materials with appropriate or different potential windows in the same electrolyte, extending the operating potential window which improves the energy density of the supercapacitors and hence, providing an effective power source with high energy density which is crucial for many applications [3,4]. This configuration of ECs provides the best performance characteristics for the device, increasing the capacity via the faradaic charge-storage mechanisms of the positive electrode, while maintaining fast charge-discharge response due to the double-layer capacitance mechanism at the negative electrode. Furthermore, in this configuration, the high over potentials for H_2 and O_2 evolution at the negative electrode (usually carbon materials) and pseudocapacitive positive electrode, extends the effective potential window of aqueous electrolytes beyond the thermodynamic limit (~1.2 V), which results in significantly higher capacitance and energy density than for symmetric ECs in aqueous electrolytes [4]. Generally, aqueous electrolytes (such as KOH or Na_2SO_4) supports high-power operation because of their high ionic

conductivity and high concentrations of ions, while providing cost and safety advantages of a water-based electrolyte compared to non-aqueous electrolytes [5,6].

Generally most ASCs ECs make use of activated carbon (AC) as the negative electrode [7] because of the anomalous pseudocapacitance mechanism at the surfaces of carbon-based electrodes when scanned at a negative potentials in aqueous electrolytes [8]. This mechanism has been attributed to "electrochemical hydrogen storage" process whereby hydrogen atoms are formed at the surface of the electrode when electrons are transferred from the carbon electrode to H_2O molecules followed by adsorption on the carbon surface according to the equations below [9,10].

$$\langle \mathrm{C} \rangle + x\mathrm{H_2O} + x\mathrm{e^-} \leftrightarrow \langle \mathrm{CH_x} \rangle + x\mathrm{OH^-} \qquad [1]$$

Where $\langle CH_x \rangle$ stands for the hydrogen inserted into the nano-textured carbon during charging and oxidized during discharging

Transition metal oxides (TMOs), conducting polymers and their corresponding composites materials are promising candidates for ECs applications and are mostly used as positive electrode [11–13]. TMOs are widely considered as positive electrode because of their inherent "pseudocapacitance" which is due to rapid and reversible electron exchange reactions at the electrode interface. These materials usually express broad charge–discharge profiles when compared with profiles generated by the double-layer capacitance [14].

Several ASC systems having broad potential window up to 2.0 V have been developed based on TMO, carbon nanotube (CNT) and activated carbon. Some of these studies include, activated carbon (AC)//manganese oxides (MnO_2) [15,16], carbon nanotube//MnO_2 [13], AC//$Ni(OH)_2$ [17]. Conducting polymers, polymer composite materials and carbon materials such as CNT have also been reported for ASC applications some of which are:

AC//conducting polymers [6,18], CoO@polypyrrole//activated carbon [19] and carbon nanotube/PANI (CNT/PANI) [20] just to mention a few.

The discovery of graphene, a two-dimensional allotrope of carbon which is considered to be a good electrode material for ECs has attracted a lot of attention due to its exceptional properties, such as large surface area, high electrical conductivity, good electrochemical stability and excellent mechanical behaviour. Several composites of graphene with TMOs or conducting polymers have been successfully prepared by various techniques as electrode materials for ECS; some of which include MnO_2//graphene [12,16,21,22], graphene-RuO_2//graphene [23], graphene-$Ni(OH)_2$//graphene [24], etc. More recently, three-dimensional (3D) flexible and conducting interconnected graphene network formed using chemical vapour deposition onto a catalytic nickel foam template have found application as electrode for ECs due to their highly conductive network and unique porous structure [25–28]. Although numerous research has been carried out so far there are still no studies reporting the fabrication of ASCs with activated graphene foam-based materials as the anode and activated carbon as the cathode in an aqueous electrolyte media.

In this work, we report a new type of ASCs based on activated graphene foam (GF) with 3D interconnected pores and activated carbon on a nickel foam current collector. Our approach for making porous nanostructures materials involves two key steps; first the production of the hydrogel and secondly activation of the hydrogel to produce the porous nanostructured material. The study investigates the hybrid ASCs consisting of a combination of AC as cathode material, activated graphene foam based materials as anode material denoted as GF/PVA-F//AC, in a 1 M Na_2SO_4 aqueous solution as electrolyte for their electrochemical performance.

2 EXPERIMENTAL

2.1 Preparation of graphene foam hydrogel

Graphene foam (GF) were prepared by chemical vapour deposition (CVD) onto a catalytic nickel foam (Alantum Innovations in Alloy Foam Munich, Germany) as reported in our previous work [27]. The three dimensional hydrogel was synthesised via microwave process. Typical, 100 mg of GF was dispersed in 10 ml of water containing 10 mg of polyvinyl alcohol (PVA) in a vial glass by ultrasonication, 0.5 ml of formaldehyde (37 wt. %) was added as additional carbon sources and 1.5 ml of hydrochloric acid (HCl) was added to the solution as a cross linker [29]. To enhance the conductivity of the hydrogel, 0.5 ml of a conducting polymer; polypyrole (PPY) was also added to the solution which also serve as additional carbon source for the composite hydrogel. In addition to this, PPY was chosen because it has been shown to have a unique pentagonal ring structure with heteroatoms such as nitrogen which might induce a doping effect on the hydrogel during the carbonization process; hence improving on the conductivity, wettability of the produced porous carbon and also maximization of the electro-active surface area for improved electrochemical performance of the composite material [30,31]. After the addition of PPY, the solution was stirred for 30 minutes to obtain a homogeneous dispersion and the resulting solution was transferred into microwave reactor chamber operated at 180 ^{o}C for 6 hours. The resulting hydrogel was washed with deionized water and dried for 6 hours.

2.2 Preparation of the activated GF-PVA/F

The as-prepared hydrogel was then soaked in aqueous KOH solution with a KOH/hydrogel mass ratio of 7 for 24 hours and dried at 120 °C for 12 hours before carbonization [32]. The composite mixture was then placed in a horizontal tube furnace ramped from room temperature to 800 ^{o}C at 10 ^{o}C/minute under argon gas flow for 1 hour of activation. This

procedure transforms the composite hydrogel into carbon materials consisting of a continuous pore network distribution. The activated material denoted as GF/PVA-F was washed with deionised water and dried at 120 ^{o}C for 12 hours after which samples were characterized.

2.3 Microstructural characterization

The surface morphologies of the as-produced carbon materials were observed by Zeiss Ultra Plus 55 field emission scanning electron microscope (FE-SEM) operated at an accelerating voltage of 2.0 kV. Raman spectroscopy measurements were carried out using a Jobin Yvon Horiba TX 6400 micro-Raman spectrometer equipped with a triple monochromator system to eliminate contributions from Rayleigh lines and using LabSpec (Ver. 5.78.24) analytical software. All the samples were analyzed with a 514 nm argon excitation laser (1.5 mW laser power on the sample to avoid thermal effects). Fourier-Transform Infrared (FTIR) spectra were recorded on a Vertex 70v (Bruker) spectrometer in the 4000-600 cm^{-1} range with 4 cm^{-1} resolution and analyzed with the Opus software and the liquid nitrogen cryosorption analysis was measured at -196 °C using Micromeritics TriStar II 3020 (version 2.00).

2.4 Electrochemical characterization

For electrode preparation best practice methods were used to obtain reliable results and draw conclusion as recommended by Stoller *et al.* [33]. The GF/PVA-F positive electrode materials and Polyvinylidene difluoride (PVDF) binder with a weight ratio of 9: 1 was homogenized in an agate mortar, dispersed in 1-methyl-2-pyrrolidinone (NMP) solvent to form a paste. This obtained paste was pressed onto nickel foam grids (1 cm x 1 cm and circular disk with diameter of 1.5 cm) which acts as a current collector and dried at 60 ^{o}C in an oven for 8 hours to ensure complete evaporation of the NMP. The negative electrode, activated carbon (from Protechnik South Africa) was also fabricated following the same procedure with 9:1 ratio of activated carbon (AC) and PVDF binder without the addition of a

conducting material such as carbon black or acetylene black. At this juncture it is worth stating that for an asymmetric cell design the potential splitting depends on the individual capacitance of both the positive and negative electrode material used.

For the asymmetric cell it is important to take into account the charge equality $(q+ = q-)$ on both electrodes since the voltage splitting depends on the capacitance of the active material in each of the electrode. Therefore, the mass have to be balanced according to charge equivalence, where $q+$ and $q-$ are the charges stored in the positive and negative electrode respectively. These charges stored are dependent on the specific capacitance (C_s), the potential window of the charge-discharge process (U) and the mass of the active electrode material (m) and can be expressed by equation 2 below [12];

$$q = C_s \times U \times m \qquad [2]$$

and in order to obtain the mass balance, equation (2) can be re-expressed as equation (3) below [12]

$$\frac{m_+}{m_-} = \frac{C_- \times U_-}{C_+ \times U_+} \qquad [3]$$

Where m_+, m_- are the masses of the positive and negative electrodes, U_- ,U_+ are the potential window of the positive and negative electrode and $C-$, $C+$ are the capacitance values of the two electrode materials.

For the fabrication of our asymmetric device the mass ratio of the positive electrode (GF/PVA-F) and the negative electrode (AC) was ($M_{AC}/M_{GF/PVA-F}$=2.1) according to the specific capacitance of the electrode materials calculated in three electrode configuration using the GF/PVA-F and AC as the working electrode, glassy carbon plate as the counter electrode and Ag/AgCl (3 M KCl) serving as the reference electrode in a 1 M Na_2SO_4

aqueous electrolyte. The electrochemical test of the asymmetric device (GF/PVA-F//AC) was carried out in a two electrode cell configuration with a mass loading of ~3 mg for the positive electrode and a mass loading of ~ 6.5 mg for the negative electrode on a nickel foam current collector with thickness of 0.2 mm and diameter of 16 mm, using a glass microfiber filter paper as the separator in the same aqueous electrolyte solution and all measurements were carried out using a Bio-logic SP-300 potentiostat. Electrochemical measurements include cyclic voltammetry (CV), galvanostatic charge-discharge (GCD) and electrochemical impedance spectroscopy (EIS). The CV tests were carried out in the potential range of 0 to 1.8 V at different scan rates ranging from 5 m Vs^{-1} to 100 m Vs^{-1}. The GCD measurements were also carried out at different current densities: from 0.5 mA cm^{-2} to 5.6 mA cm^{-2} and the EIS studies were carried out in the frequency range of 100 kHz- 0.01 Hz with 2 mV AC amplitude. The areal specific capacitance in (F cm^{-2}) was calculated from the charge-discharge curves according to equations 4 and 5 below.

$$C = I\Delta t/\Delta U \quad [4]$$

$$C_s = C/S \quad [5]$$

Where C is the total capacitance, I is the discharge current (A), Δt is the discharge time (s), ΔU is the applied potential window in (V) after the IR drop has been subtracted and S is the working surface area of the sample in (cm). The energy (W h cm^{-2}) and power (W cm^{-2}) densities of the device were calculated from the specific capacitance using equations 6 and 7 respectively.

$$E_{density} = 0.5C_s(\Delta U)^2 \quad [6]$$

$$P_{density} = E/t \quad [7]$$

ΔU is the applied potential window in (V)after the IR drop has been subtracted, C_s is the specific capacitance and t is the discharge time measured in hours.

3 RESULTS AND DISCUSSION

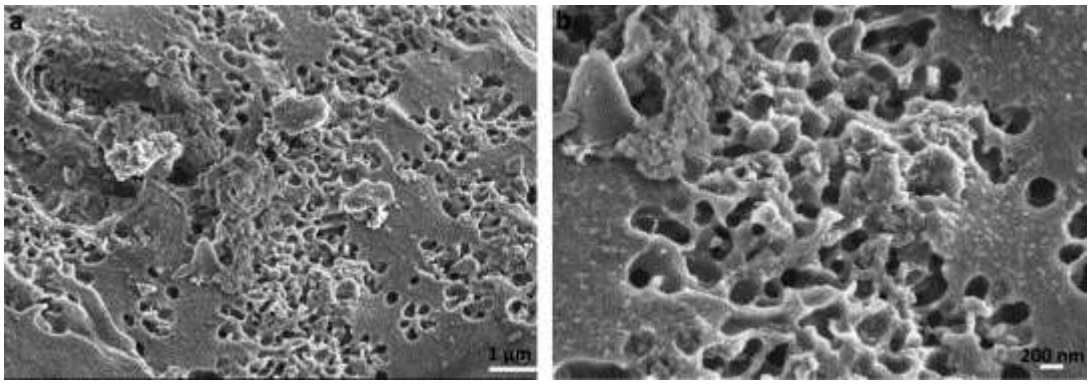

Figure 1 SEM images (a) low magnification and (b) high magnification of GF/PVA-F.

Figure 1 (a) and (b) present low and high magnification SEM images of the produced material GF/PVA-F respectively. The material exhibits a spongy-like structure containing irregular porous cavities with a substantial amount of macropores. From the high magnification image, it appears that these cavities penetrate deep into the material in non-uniform distribution pattern and contain some agglomeration derived from a large volume expansion in the activation process with KOH. The activation of materials using KOH takes place according to the following reaction;

$$6KOH + C \leftrightarrow 2K + 3H_2 + 2K_2CO_3 \quad [8]$$

This is followed by decomposition of K_2CO_3 and/or reaction of K_2CO_3 with carbon [32]. Usually, the KOH activation process generates porous structures such as micropores, mesopores and macropores which could facilitate a rapid mass diffusion during electrochemical operation leading to enhanced supercapacitor performance [34]. It is worth stating that the surface of the macropores (>50 nm) makes virtually no contribution to the total capacitance, but act as the ion buffering reservoir, while micropores (<2 nm in size)

serve as the ion traps for energy storage, and mesopores (2<50 nm) act as the ion transport pathways for power delivery [35].

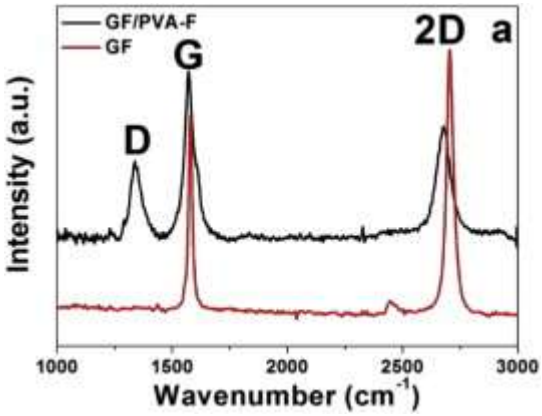

Figure 2 Raman spectra of GF and GF/PVA-F.

Raman spectroscopy has been shown to be a useful tool for the characterization of structural defects in carbon materials [36]. Figure 2 represents typical Raman spectrum of the graphene foam (GF) and the as-prepared activated materials. The Raman spectrum of the GF shows prominent peaks at 1582.2 cm^{-1} and 2705.7 cm^{-1}, which corresponds to the G and 2D-bands of graphitic material without D-peak related to disorder at 1350 cm^{-1}. The relative intensity 2D/G ratio of 1.2 and FWHM of 38.8 cm^{-1} were attributed to few layer graphene. This evidences that the GF produced was of good quality. The spectrum of the activated material GF/PVA-F show pronounced D-peak at ~1350 cm^{-1} with additional peaks at ~1582 cm^{-1} and ~2692 cm^{-1} which also correspond to the G and 2D-bands of graphitic material. The appearance of the D-peak after activation may be due to the activation process or to interaction between the PVA and GF, which introduces a strain effect and results in the shift of the 2D-peak position as observed, this could also lead to the appearance of the disorder peak [37].

To obtain information about the surface area as well as the micro and mesoporous nature of the as-produced material, Brunauer–Emmett–Teller (BET) was performed and the result is

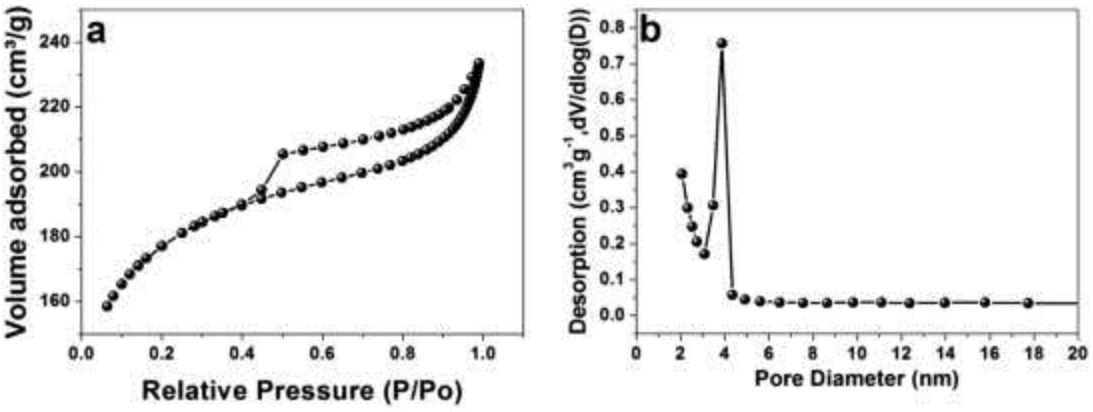

Figure 3 (a) Nitrogen adsorption and desorption isotherm and (b) pore size distribution for GF/PVA-F.

shown in Figure 3. The nitrogen adsorption and desorption show type IV isotherm (Figure 3 (a)) and a corresponding specific surface area value of 610 m^2g^{-1} was obtained. The hysteresis loop at a relative pressure P/P_0 of about 0.45–1.0 is attributed to capillary condensation of the mesopores in the solid material [38]. The pore size distribution is shown in Figure 3 (b). The material shows a pore size distribution in the range of 20 nm and the average size centred at about 4 nm is ascribed to mesopores present in the sample. The increase in the pore distribution below 2 nm may indicate the existence of micropore in this sample. From these observations we conclude that the large specific surface area and the large composition of mesopores which provides a more suitable and favourable pathways for electrolyte penetration could facilitate fast ion transport and give rise to the excellent electrochemical property of the electrode material which is beneficial for high performance supercapacitors [39].

The characteristic electrochemical properties of the assembled ASC cell are shown in Figure 4. In Figure 4 (a), a schematic illustration of the asymmetric cell with the GF/PVA-F as positive electrode and AC as negative electrode with a glass microfiber filter paper as the separator and 1 M Na_2SO_4 solution serving as the electrolyte is presented as well as the

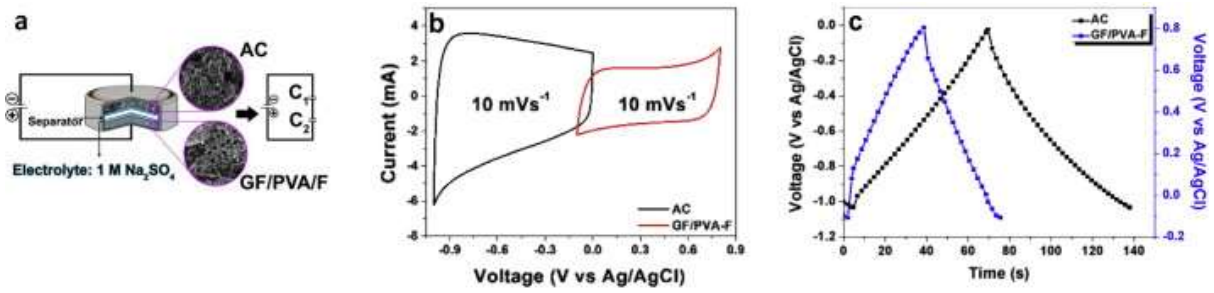

Figure 4 (a) schematic diagram of the fabricated asymmetric device showing GF/PVA-F as positive electrode and AC as negative electrode (b) CV curves of GF/PVA-F and AC electrode in a three electrode configuration showing different potential windows at a scan rate of 10 mV s^{-1} (c) The galvanostatic charge/discharge curves of GF/PVA-F and AC at a current density of 3.4 mA cm^{-2}.

equivalent circuit with two capacitor in series. Figure 4 (b) presents the CV of the GF/PVA-F and AC half-cell electrodes measured in a three electrode configuration at different potential window between -1 V to 0.8 V vs Ag/AgCl at scan rate of 10 mV s^{-1}. The CV curves are quasi rectangular meaning ideal capacitive behaviour. The galvanostatic charge/discharge curve of both samples are shown in 4 (c) and it can be observed that they are symmetrical and linear suggesting a rapid and excellent electrochemical reversibility. From these curves the specific capacitance for GF/PVA-F and AC were calculated from equation (1) to be 0.12 F cm^{-2} and 0.28 F cm^{-2} respectively.

The CV curves of the optimised GF/PVA-F //AC asymmetric cell are shown in Figure 5 (a) at a scan rate of 5 and 10 m Vs^{-1}. The fabricated cell operates at an extended potential window of 1.8 V and the curves show ideal capacitive behaviour with rectangular CV shapes. Figure 5 (b) shows the CV curves of the optimised asymmetric cell at different scan rates ranging from 5 to 100 mV s^{-1}. The CV curves still maintain their rectangular shape with increasing scan rate indicating fast ion charge propagation at the interface between the electrode and electrolyte for an efficient double layer capacitor.

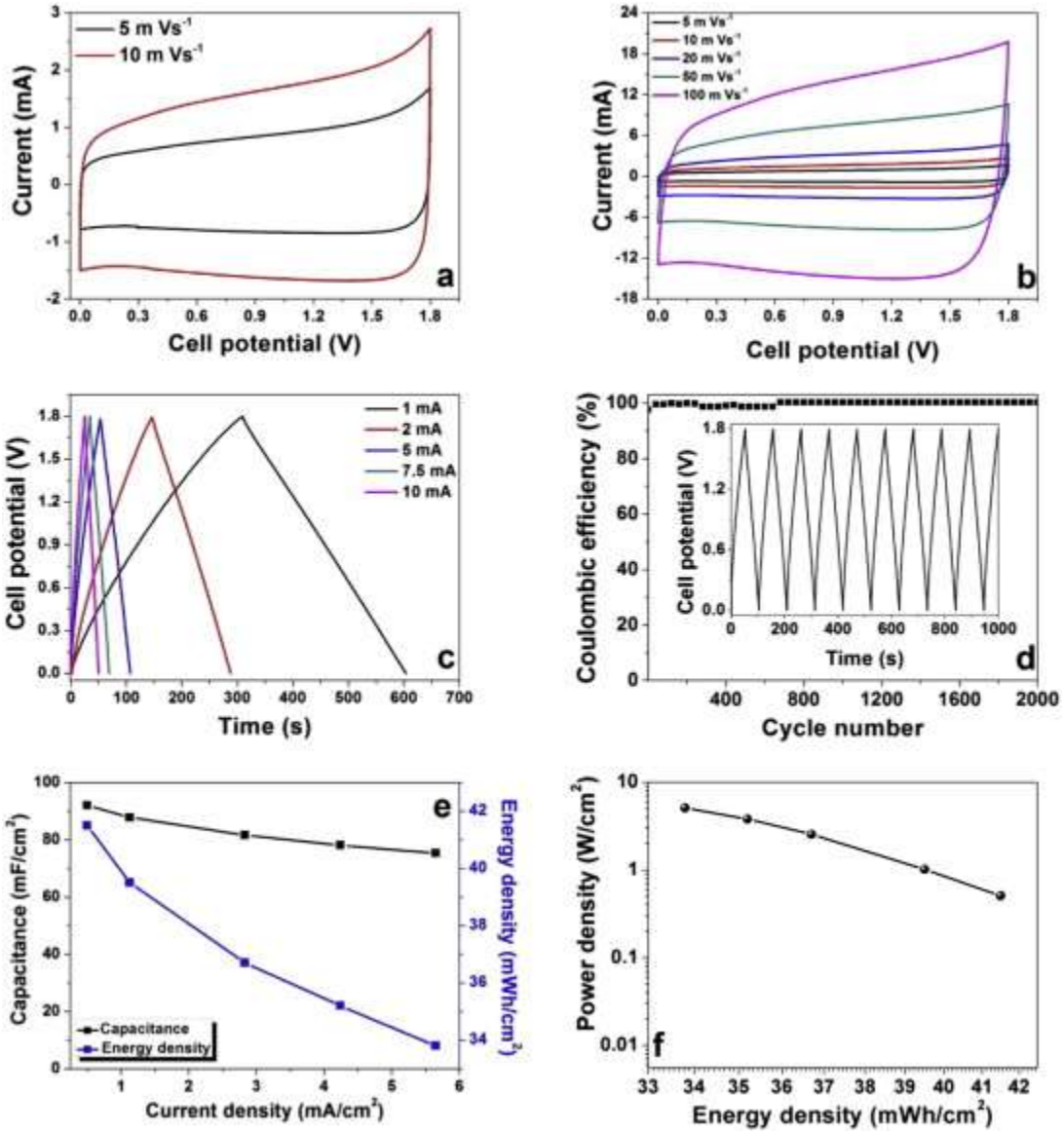

Figure 5 (a) CV curves at scan rates of 5 and 10 m Vs^{-1}, (b) CV curves from scan rates of 5 to 100 m Vs^{-1} (c), The galvanostatic charge/discharge curves at different currents, (d) Cycle stability at a constant current of 5 mA (e) Specific capacitance and energy density as a function of current density (f) Ragone plot of the asymmetric cell based on GF/PVA-F as positive electrode and AC as negative electrode.

Figure 5 (c) presents the galvanostatic charge-discharge curves of the asymmetric cell at different current densities from 0.5 mA cm^{-2} (0.1 A g^{-1}) to 5.6 mA cm^{-2} (1 A g^{-1}) showing a typical triangular shape proportional to the charged or discharged times. The nature of the galvanostatic plot indicates a rapid current-voltage response which corresponds to ideal capacitive characteristic of the cell as confirmed from the CV above. Furthermore, the

voltage drop (IR) observed from the beginning of the discharge is negligible suggesting a low equivalent series resistance (ESR) for the asymmetric cell. From the discharge curves, the specific areal capacitance of the cell was calculated to be 92 mF cm^{-2} at a current density of 0.5 mA cm^{-2}. Cycling test (charge and discharge) was performed to evaluated to the stability of the device and the result is shown in Figure 5 (d) which shows the coulombic efficiency of the asymmetric cell upon charging-discharging at a current density of 2.8 mA cm^{-2}. The cell undergoes 2 % drop from its initial capacitance over the first 500 cycles and keeps a constant value afterwards to 2000 cycles maintaining almost 100 % of the available capacitance. This we attribute to the uniform pore distribution which functions as a series of channels and may promote ion intercalation into these pores, creating more nano-pores after many CD cycle leading to increase in the efficiency. The initial decay may be related to the loss of adhesion between some of the active materials with the current collector during the continuous cycling process [40]. The specific capacitance and energy density are plotted as a function of current density and are shown in Figure 5 (e). The decrease in capacitance value as the current density increases could be due to the presence of redox reaction of electrosorbed hydrogen and oxygen containing functional groups in the matrix of the electrode material [41]. However, at a high current density of 5.8 mA cm^{-2}, the C_s of the device still retains the value of 75 mF cm^{-2}.

The Ragone plot of the asymmetric device is shown in Figure 5 (f). The power and energy densities values have been calculated from the discharge curves at different current densities and it was observed that the energy density slowly decreases with increasing power density. At a power density of 5 W cm^{-2}, (174 W kg^{-1}) the energy density of the device remained at a value of 34 mWh cm^{-2} (14.2 Wh kg^{-1}) suggesting good rate capability and this is due to the extended potential window (1.8 V) of the asymmetric device. These values are reasonable

and comparable to previous asymmetric device based on carbon materials as negative electrode and metals oxide or polymer based materials as positive electrode [5,12,18,42].

Overall, the excellent electrochemical behaviour of the asymmetric device could be attributed to the increased potential window which leads to an increase in energy density since the energy is a function of the square of the voltage. Furthermore, the highly interconnected porous structure of the electrode materials serve as channels (short diffusion pathway) for faster diffusion which favours a rapid fast charge transportation and higher Na^+ ion mobility improving fast and efficient propagation leading to low solution resistance (R_s) and charge transfer resistance (R_{ct}) values and hence increased electrochemical performance.

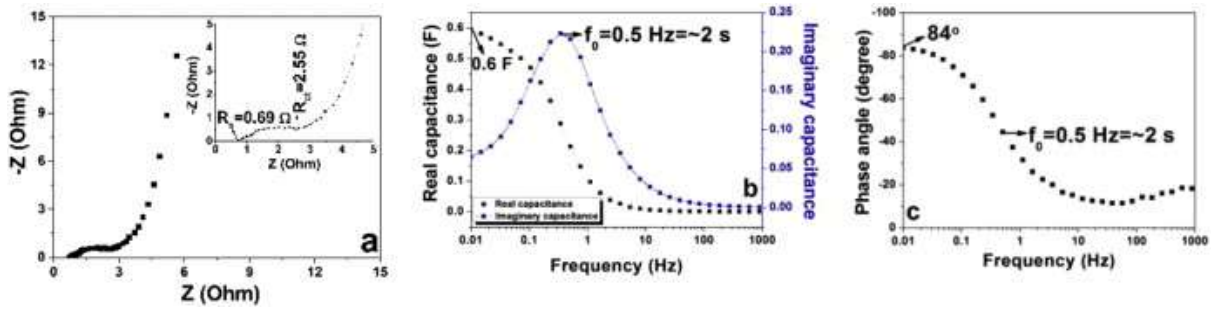

Figure 6 EIS characteristics of the cells: (a) Nyquist plot with inset showing the partial semicircle, (b) the real and the imaginary part of the cells capacitance against frequency, (c) the phase angle versus frequency.

Electrochemical impedance spectroscopy (EIS) analysis was performed to confirm the fast ion transport (diffusion) of the hybrid electrodes as shown in Figure 6 (a). The Nyquist plot shows a typical capacitive shape with the inset to the figure showing an arc at the high frequency and a nearly vertical line in the low frequency region which represents the diffusion behaviour of the hybrid electrodes, thus displaying a pure capacitive behaviour of the asymmetric device. In the high frequency region (100 kHz) the intercept on the real part of the impedance (x-axis) denoted as R_S represents ESR which consists of the electrode material, the ionic resistance of electrolyte and contact resistance at the interface between the material and current collector [43]. The value obtained is ~ 0.7 Ω which suggest that the

current flows easily through the electrode /electrolyte/electrode configuration without significant dissipation [41]. This means that the ions from the electrolyte rapidly flow through the electrode/electrolyte which could be attributed to the mobility of the Na^+ cations and the porous structure of the electrode materials. Also, the inconspicuous arc (semicircle) in the high to mid frequency, which corresponds to the interfacial charge transfer resistance R_{ct} of 2.5 Ω suggests a good distribution and connection of ions at the electrode/electrolyte interface. The slope of the 45° portion of the curve is referred to as the Warburg resistance and is attributed to the frequency dependency on the ion diffusion from the electrolyte to the surface of the electrode [44]. The capacitance (real and imaginary parts) as a function of frequency is shown in Figure 6 (b). A small frequency dependency in the range of (0.01-0.5 Hz) and a capacitance of 0.6 F was observed from the real part of the capacitance. Also, it is observed that the imaginary capacitance passes through a maximum frequency f_o (0.5 Hz, transition frequency between a pure capacitive and a pure resistive behaviour) which defines the relaxation time $\tau=1/f_o= 2\ s$ suggesting that the cell could reach its maximum capacitance at a very fast recharging time of 2 s. The fast frequency response of the asymmetric device was attributed to the porous structure of the electrode material which provides full accessibility to the ions from the electrolyte leading to faster diffusion rates. In Figure 6 (c) the dependence of the phase angle on the frequency of the asymmetric device is shown with a phase angle of about -84° which is close to -90° for ideal capacitors suggesting that the device is a good capacitor.

4 CONCLUSION

We have demonstrated a simple approach to effectively produce novel 3D porous materials with highly interconnected cavities based on graphene foam and polyvinyl alcohol, and assembled asymmetrical supercapacitor cell by coupling the porous GF/PVA-F as positive electrode and AC as negative electrode in highly safe Na_2SO_4 aqueous electrolyte. This

approach is realistic, reliable and scalable for production of porous material to the industrial scale for real time applications. The asymmetric device showed good capacitance, energy and power densities values operating within a potential window of 1.8 V and also exhibited excellent cycle life. The robust 3D nanoarchitecture of the porous material avoids disintegration decay and hence leads to improved performance of the device. This material is highly promising for application in high performance energy storage systems. Improvement of the electrodes such as optimization of device configuration, decreasing the interspaces between the electrodes and rational selection electrolyte will further enhance the performance of the device.

ACKNOWLEDGEMENTS

This work is based upon research supported by the South African Research Chairs Initiative (SARChi) in carbon Technology and Matarials of the Department of Science and Technology (DST) and the National Research Foundation (NRF). Any opinion, findings and conclusions or recommendations expressed in this work are those of authors and therefore the NRF and DST do not accept any liability with regard thereto. A. Bello, acknowledges University of Pretoria financial support for his PostDoc fellowship, while D. Y. Momodu and F. Barzegar acknowledge financial support from University of Pretoria and NRF for their PhD bursaries.

References

[1] B. Conway, Electrochemical Supercapacitors: Scientific Fundamentals and Technological Applications (POD), Kluwer Academic/Plenum: New York, 1999.

[2] P. Simon, Y. Gogotsi, Nat. Mater. 7 (2008) 845.

[3] J.W. Long, D. Bélanger, T. Brousse, W. Sugimoto, M.B. Sassin, O. Crosnier, Mrs Bull 36 (2011) 513.

[4] W.G. Pell, B.E. Conway, J. Power Sources 136 (2004) 334.

[5] J.-Y. Luo, Y.-Y. Xia, J. Power Sources 186 (2009) 224.

[6] V. Khomenko, E. Raymundo-Pinero, E. Frackowiak, F. Beguin, Appl. Phys. A 82 (2006) 567.

[7] N.W. Duffy, W. Baldsing, A.G. Pandolfo, Electrochim. Acta 54 (2008) 535.

[8] F. Béguin, K. Kierzek, M. Friebe, A. Jankowska, J. Machnikowski, K. Jurewicz, E. Frackowiak, Electrochim. Acta 51 (2006) 2161.

[9] F. Béguin, M. Friebe, K. Jurewicz, C. Vix-Guterl, J. Dentzer, E. Frackowiak, Carbon 44 (2006) 2392.

[10] D. Qu, J. Power Sources 179 (2008) 310.

[11] Z. Algharaibeh, X. Liu, P.G. Pickup, J. Power Sources 187 (2009) 640.

[12] V. Khomenko, E. Raymundo-Pinero, F. Béguin, J. Power Sources 153 (2006) 183.

[13] H. Jiang, C. Li, T. Sun, J. Ma, Nanoscale 4 (2012) 807.

[14] X. Zhao, B.M. Sánchez, P.J. Dobson, P.S. Grant, Nanoscale 3 (2011) 839.

[15] M.S. Hong, S.H. Lee, S.W. Kim, Electrochem. Solid-State Lett. 5 (2002) A227.

[16] Z. Fan, J. Yan, T. Wei, L. Zhi, G. Ning, T. Li, F. Wei, Adv. Funct. Mater. 21 (2011) 2366.

[17] S. Nohara, T. Asahina, H. Wada, N. Furukawa, H. Inoue, N. Sugoh, H. Iwasaki, C. Iwakura, J. Power Sources 157 (2006) 605.

[18] A. Laforgue, P. Simon, J.F. Fauvarque, M. Mastragostino, F. Soavi, J.F. Sarrau, P. Lailler, M. Conte, E. Rossi, S. Saguatti, J. Electrochem. Soc. 150 (2003) A645.

[19] C. Zhou, Y. Zhang, Y. Li, J. Liu, Nano Lett. 13 (2013) 2078.

[20] T.-M. Wu, Y.-W. Lin, C.-S. Liao, Carbon 43 (2005) 734.

[21] H. Gao, F. Xiao, C.B. Ching, H. Duan, ACS Appl. Mater. Interfaces 4 (2012) 2801.

[22] Z. Lei, J. Zhang, X.S. Zhao, J. Mater. Chem. 22 (2012) 153.

[23] B.G. Choi, S.-J. Chang, H.-W. Kang, C.P. Park, H.J. Kim, W.H. Hong, S. Lee, Y.S. Huh, Nanoscale 4 (2012) 4983.

[24] J. Yan, Z. Fan, W. Sun, G. Ning, T. Wei, Q. Zhang, R. Zhang, L. Zhi, F. Wei, Adv. Funct. Mater. 22 (2012) 2632.

[25] Y. Chen, X. Zhang, P. Yu, Y. Ma, J. Power Sources 195 (2010) 3031.

[26] H. Ji, L. Zhang, M.T.M. Pettes, H. Li, S. Chen, L. Shi, R. Piner, R.S. Ruoff, Nano Lett. 12 (2012) 2446.

[27] A. Bello, O.O. Fashedemi, J.N. Lekitima, M. Fabiane, D. Dodoo-Arhin, K.I. Ozoemena, Y. Gogotsi, A.T. Charlie Johnson, N. Manyala, AIP Adv. 3 (2013) 82118.

[28] H. Wang, H. Yi, X. Chen, X. Wang, J. Mater. Chem. A 2 (2014) 3223.

[29] L. Zhang, F. Zhang, X. Yang, G. Long, Y. Wu, T. Zhang, K. Leng, Y. Huang, Y. Ma, A. Yu, C. Yongsheng, Sci. Rep. 3 (2013).

[30] L.-F. Chen, X.-D. Zhang, H.-W. Liang, M. Kong, Q.-F. Guan, P. Chen, Z.-Y. Wu, S.-H. Yu, ACS Nano 6 (2012) 7092.

[31] L. Qie, W. Chen, H. Xu, X. Xiong, Y. Jiang, F. Zou, X. Hu, Y. Xin, Z. Zhang, Y. Huang, Energy Environ. Sci. 6 (2013) 2497.

[32] Y. Zhu, S. Murali, M.D. Stoller, K.J. Ganesh, W. Cai, P.J. Ferreira, A. Pirkle, R.M. Wallace, K.A. Cychosz, M. Thommes, D. Su, E.A. Stach, R.S. Ruoff, Science 332 (2011) 1537.

[33] M.D. Stoller, R.S. Ruoff, Energy Environ. Sci. 3 (2010) 1294.

[34] X. Ma, M. Liu, L. Gan, Y. Zhao, L. Chen, J. Solid State Electrochem. 17 (2013) 2293.

[35] M. Zhi, F. Yang, F. Meng, M. Li, A. Manivannan, N. Wu, ACS Sustain. Chem. Eng. (2014).

[36] M.A. Pimenta, G. Dresselhaus, M.S. Dresselhaus, L.G. Cancado, A. Jorio, R. Saito, Phys. Chem. Chem. Phys. 9 (2007) 1276.

[37] Z. Ni, T. Yu, Z. Luo, Y. Wang, L. Liu, ACS Nano 3 (2009) 569.

[38] M. Liu, L. Gan, W. Xiong, Z. Xu, D. Zhu, L. Chen, J. Mater. Chem. A 2 (2014) 2555.

[39] Y. Lv, L. Gan, M. Liu, W. Xiong, Z. Xu, D. Zhu, D.S. Wright, J. Power Sources 209 (2012) 152.

[40] J.N. Lekitima, K.I. Ozoemena, C.J. Jafta, N. Kobayashi, Y. Song, D. Tong, S. Chen, M. Oyama, J. Mater. Chem. A 1 (2013) 2821.

[41] K. Fic, G. Lota, M. Meller, E. Frackowiak, Energy Environ. Sci. 5 (2012) 5842.

[42] J. Zhang, J. Jiang, H. Li, X.S. Zhao, Energy Environ. Sci. 4 (2011) 4009.

[43] B.G. Choi, J. Hong, W.H. Hong, P.T. Hammond, H. Park, ACS Nano 5 (2011) 7205.

[44] M.D. Stoller, S. Park, Y. Zhu, J. An, R.S. Ruoff, Nano Lett. 8 (2008) 3498.